J Adv Ceram

Research Article

Excellent comprehensive piezoelectric performances of SiC-doped BCTZ-based lead-free piezoelectric ceramics

Aihui Yang[1], Yu Huan[1,✉], Qingying Wang[1], Ting Wang[2,✉], Yuanhui Su[1], Tao Wei[1]

Cite this article: Yang A, Huan Y, Wang Q, et al. *J Adv Ceram* 2025, **14**(4): 9221054. https://doi.org/10.26599/JAC.2025.9221054

ABSTRACT: With increasing awareness of environmental protection, the electrical performance and sintering process of lead-free piezoelectric ceramics are continuously optimized to replace lead-based materials. Exploring an appropriate doping strategy is believed to achieve concurrent improvements in lead-free piezoelectric ceramics. In this work, SiC was selected to optimize the phase structure, defect configuration, and morphology of $(Ba_{0.85}Ca_{0.15})(Zr_{0.1}Ti_{0.9})O_3$ (BCTZ) lead-free piezoelectric ceramics. On the one hand, SiC could promote the sintering process and grain growth due to its excellent thermal conductivity, resulting in the compactness and outstanding insulation of the doped ceramics. On the other hand, the incorporation of Si^{4+} in the B-site of the ABO_3 lattice not only deforms the crystal structure and enhances the lattice distortion but also reduces the oxygen vacancy concentration and increases the charge carrier activation energy. As a result, excellent comprehensive piezoelectric responses of piezoelectric coefficient (d_{33}) = 638 pC/N, inverse piezoelectric coefficient (d_{33}*) = 1048 pm/V, planar electromechanical coupling coefficient (k_p) = 58.21%, and Curie temperature (T_c) of ~95 °C were achieved with the optimized composition. Our work demonstrated that SiC-doped BCTZ-based ceramics are potential candidates for replacing lead-based piezoceramics.

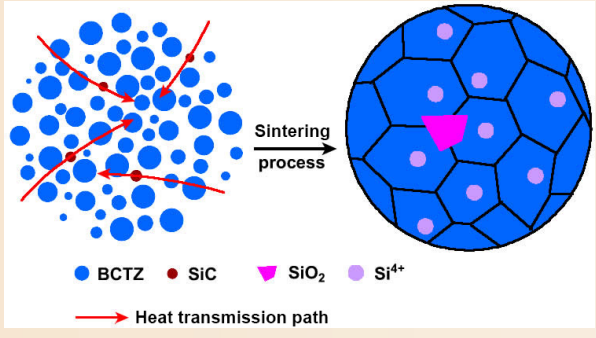

KEYWORDS: $(Ba_{0.85}Ca_{0.15})(Zr_{0.1}Ti_{0.9})O_3$ (BCTZ) piezoceramics; SiC doping; sintering temperature; crystal structure; excellent piezoelectric properties

1 Introduction

Piezoelectric ceramics are functional materials that can achieve mutual energy conversion between mechanical energy and electrical energy. They have been widely fabricated into actuators, transducers, and sensors and are used in aerospace, daily production, information communication, etc. [1–4]. Over the past few decades, lead-based piezoelectric ceramics have been popularly applied because of their excellent piezoelectric performance. However, lead is poisonous to the environment and human health. To respond to the requirements of national environmental protection, researchers have focused more attention and development efforts on lead-free piezoelectric ceramics in recent years [5,6]. Among these alternatives, $BaTiO_3$ (BT)-based piezoelectric ceramics are among the most promising candidates because they have emerged as promising candidates because of their good dielectric properties and excellent solid solubility compared with other perovskites [7,8]. In particular, a $Ba(Zr_{0.2}Ti_{0.8})O_3$–$x(Ba_{0.7}Ca_{0.3})TiO_3$ system with an excellent piezoelectric coefficient (d_{33}) of 620 pC/N was explored by Liu and Ren [9], which greatly accelerated the development and application of BT-based ceramics. However, the ultrahigh sintering temperature of > 1500 °C and relatively low comprehensive piezoelectric performance compared with those of commercial lead-based piezoelectric ceramics still hinder their practical application.

One of the most common methods to improve the piezoelectric response is to construct a morphotropic phase boundary (MPB) at room temperature through appropriate doping strategies or the incorporation of second-phase perovskites. For example, Chen *et al.* [10] studied the multiphase region around room temperature in a Li-doped $(Ba_{0.85}Ca_{0.15})(Zr_{0.1}Ti_{0.9})O_3$ (BCTZ) ceramic system and reported excellent piezoelectric properties of d_{33} = 493 pC/N and planar electromechanical coupling coefficient (k_p = 0.47). Unfortunately, the Curie temperature (T_c) decreases from ~100 to 60 °C, which severely deteriorates the thermal stability. The secondary phase $SiTO_3$ was incorporated into $(Ba_{0.85}Ca_{0.15})(Ti_{0.9}Zr_{0.08}Sn_{0.02})O_3$ ceramics to realize rhombohedral–orthorhombic–tetragonal multiphase coexistence and achieved excellent d_{33} of 398 pC/N, accompanied by a rapid reduction in T_c

[1] School of Material Science and Engineering, University of Jinan, Jinan 250022, China. [2] Guangdong Key Laboratory of Electronic Functional Materials and Devices, Huizhou University, Huizhou 516007, China.

✉ Corresponding authors. E-mail: Y. Huan, mse_huany@ujn.edu.cn; T. Wang, twang-hawk@foxmail.com

Received: December 20, 2024; Revised: February 24, 2025; Accepted: February 24, 2025

of ~60 °C [11]. The main reason is that the sufficient diffusion of heterogeneous elements into the ABO_3 lattice flattens the Gibbs free energy among these ferroelectric phases and thus leads to flexible polarization switching [12].

Advanced sintering processes [13,14] and the addition of sintering aids [12,15] are usually carried out to reduce the sintering temperature of BT-based ceramics. The former would generate a large manufacturing cost and is difficult to promote. The sintering aids, such as LiF, CuO, and MnO_2, can effectively reduce the sintering temperature through the generated liquid phase with a low melting point [16,17]. However, this usually results in a severely degraded piezoelectric response because the formed secondary liquid phase does not exhibit piezoelectricity. For instance, adding CuO to $Ba_{0.85}Ca_{0.15}Ti_{0.9}Zr_{0.1}O_3$ lead-free piezoelectric ceramics reduces the sintering temperature from 1500 to 1400 °C but leads to a decrease in d_{33} from 360 to 225 pC/N [17].

Although doping is still a common and effective method for optimizing performance and preparation technology, it is still difficult to achieve excellent comprehensive piezoelectric performance simultaneously with a low sintering temperature. In this work, SiC was selected to optimize the BCTZ ceramics. On the one hand, the doping of SiC could promote the sintering process and compactness of ceramics because of its excellent thermal conductivity. On the other hand, Si^{4+} entered the B-site of the ABO_3 lattice, changing the crystal structure and causing lattice distortion with increasing SiC content. As a result, the optimized composition achieved the best piezoelectric performance of d_{33} = 638 pC/N and d_{33}* = 1048 pm/V when the SiC doping amount was 0.1 mol%.

2 Experimental

$(Ba_{0.85}Ca_{0.15})(Zr_{0.1}Ti_{0.9})O_3$–$x$ mol% SiC (BCTZ–xSiC for abbreviations; x = 0, 0.05, 0.1, 0.15, and 0.2) ceramics were synthesized via the conventional solid-phase reaction method. Analytically pure powders of $BaCO_3$ (> 99%), $CaCO_3$ (> 99%), TiO_2 (> 99%), $BaZrO_3$ (> 99%), and SiC (> 99%) were purchased from Shanghai Macklin Biochemical Co., Ltd., China. After the alkali metal carbonate was dried, the raw materials were weighed according to the nominal stoichiometric composition and ball-milled with ethanol for 12 h. The mixed chemicals were subsequently dried and presintered in an alumina crucible at 1150 °C for 3 h and then milled again for 12 h. After being dried and mixed with polyethylene butyraldehyde (PVB; 5 wt% alcohol solution), the powders were pressed into pellets with a diameter of 10 mm and a thickness of 1 mm under a uniaxial pressure of 4 MPa. The green ceramics were heated at 600 °C for 3 h to remove PVB and then sintered at 1400–1460 °C for 2 h. The sintered sample was coated with silver on both sides, fired at 600 °C for 10 min, and finally poled under an electric field of 3 kV/mm for 30 min.

The crystal structure of the ceramics was determined via an X-ray diffractometer (XRD; SmartLab, Rigaku, Japan) with a Cu Kα. The microstructures of the samples were observed by a scanning electron microscope (SEM; LEO-1530, OberkoChen, Germany). Transmission electron microscopy (TEM), high-resolution transmission electron microscopy (HRTEM), and selected area electron diffraction (SAED) were carried out on an electron microscope (2100Plus, JEOL, Japan) at 200 kV after the ceramics were polished and then thinned via an ion thinning instrument (Gatan691, Gatan, USA). Raman spectra in the range of 100–1000 cm^{-1} were collected via 632 nm radiation on a Raman microscope spectrometer (LabRAM HR Evolution, Horiba, France). Information on the oxygen vacancy and valence state of silicon was acquired via an X-ray photoelectron spectroscope (XPS; ESCALab 250 Xi, Thermo Fisher Scientific, USA). The density of the ceramics was measured via the Archimedes method in distilled water. The quasistatic d_{33} of the poled ceramics was measured with a quasistatic d_{33} meter (ZJ-3A, Chinese Academy of Sciences, China). The planar k_p, permittivity (ε_r), and dielectric loss (tanδ) at 1 kHz were determined via an impedance analyzer (Agilent 4294 A, Agilent, USA). The dielectric performance was tested with a precision LCR meter (E4990A, Keysight, USA) from −50 to 200 °C. Polarization hysteresis (P–E) loops and strain-electric (S–E) field curves at 1 Hz were measured via a ferroelectric analyzer (aixACCT TF Analyzer 3000, Aachen, Germany). The impedance and electrical modulus spectra over frequencies from 20 Hz to 1 MHz under root mean square voltage (V_{rms}) of 100 mV AC signal were measured by an impedance analyzer (Agilent 4294 A, Agilent, USA).

3 Results and discussion

The grain sizes of the BCTZ–xSiC ceramics were investigated via SEM, as shown in Figs. 1(a)–1(e). The corresponding grain size distributions and sintering temperatures are presented in the insets. The average grain size and relative density (measured via the Archimedes method in distilled water) as a function of x are shown in Fig. 1(f). The relative density of all the ceramic samples was greater than 97%, which was responsible for their excellent electrical properties. In addition, with an increasing doping amount, the grain size first increased but then decreased, reaching a maximum value of 12.57 μm at x = 0.1. Owing to the excellent thermal conductivity of SiC (300–500 W/(m·K)) [18] compared with $BaTiO_3$ (2–15 W/(m·K)) [19], SiC could reduce the sintering temperature, promote grain growth, and improve the compactness of the sample as a sintering aid. When the doping amount increased to more than 0.1 mol%, some of the SiC particles gathered at the grain boundaries, inhibiting grain growth and reducing the grain size. The grain size had an important influence on the piezoelectric properties. On the one hand, the large grain size corresponded to the low content of non ferroelectric grain boundaries, which was attributed to the enhanced piezoelectric properties, considering that the grain boundaries had no contribution to the piezoelectric properties [20]. In addition, the SiC located at the grain boundaries could improve the mechanical properties and thus enhance the electrical properties [21]. On the other hand, with increasing grain size, the ferroelectric domain size increases, which is beneficial for excellent piezoelectric properties [22,23]. To confirm the composition distribution of the ceramics, the local microstructure of the ceramics and the corresponding detailed elemental distribution images were obtained. As shown in Figs. 1(g) and 1(h) that Si was evenly distributed in the BCTZ–0.1SiC ceramic, which indicated that Si entered the lattice of the ceramics. Moreover, Si was enriched in the BCTZ–0.2SiC ceramic, indicating that a secondary phase with a grain size of approximately 10 μm appeared and that some Si did not enter the lattice in the BCTZ–0.2SiC ceramic, as displayed in Figs. 1(i) and 1(j). The raw SiC particles had an average grain size of 20–50 nm and good crystallinity, as shown by the TEM and HRTEM images in Fig. S1 in the Electronic Supplementary Material (ESM). This demonstrated that the SiC easily grew during the sintering process. Except for Si, the other elements were evenly distributed without any enrichment, indicating that the other elements were dissolved into the lattice, as shown in Fig. S2 in the ESM.

Domain wall motion makes a significant extrinsic contribution to piezoelectric properties. Therefore, TEM of the BCTZ–0.1SiC

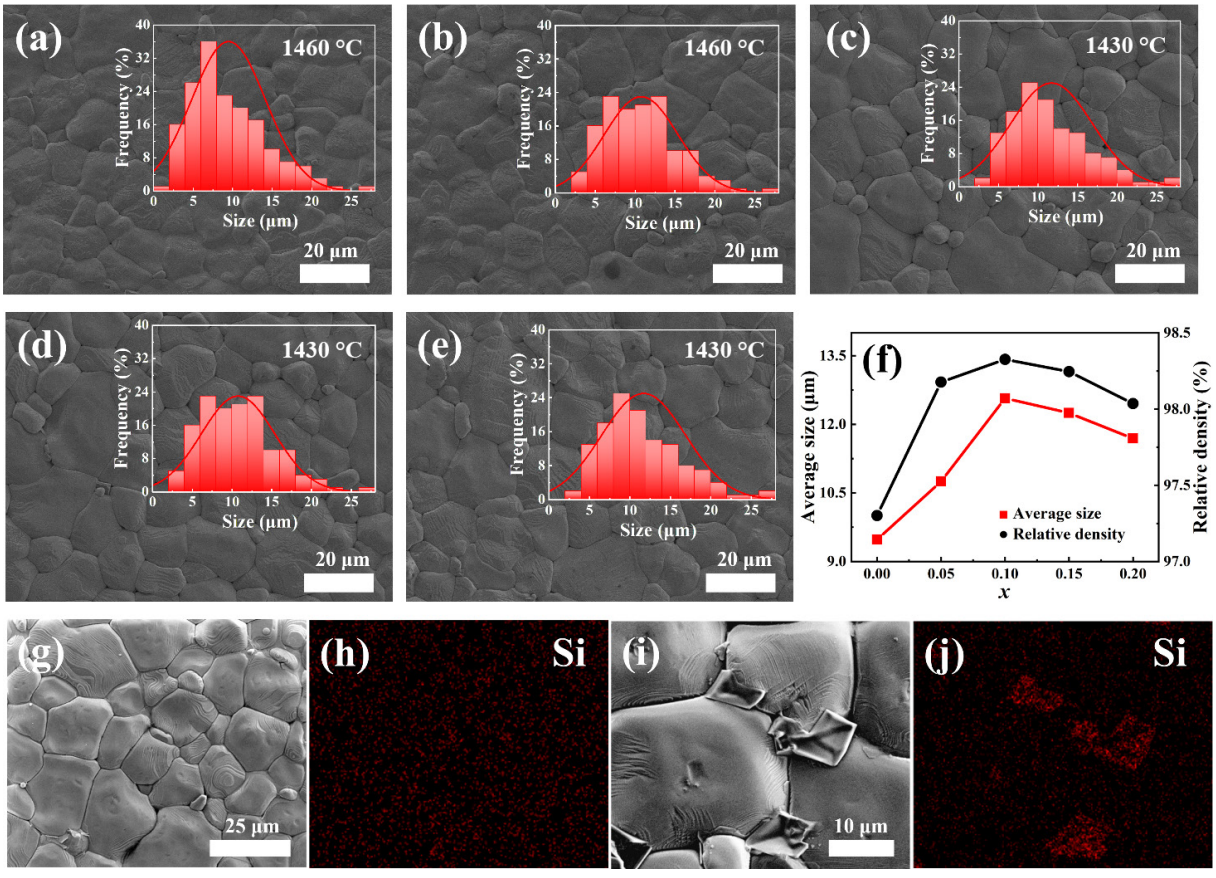

Fig. 1 SEM images of (a) BCTZ–0SiC, (b) BCTZ–0.05SiC, (c) BCTZ–0.1SiC, (d) BCTZ–0.15SiC, and (e) BCTZ–0.2SiC samples. (f) Average grain size and relative density of BCTZ–*x*SiC as a function of *x*. (g) SEM surface image and (h) Si elemental distribution map of BCTZ–0.1SiC sample. (i) SEM surface image and (j) Si elemental distribution map of BCTZ–0.2SiC sample.

ceramic samples was carried out to characterize the domain configuration, as shown in Fig. 2. Strip-layered and herringbone domain clusters were observed in the samples, with average sizes of approximately 80–300 nm, as shown in Figs. 2(a) and 2(b). The refined domain configurations could facilitate the polarization orientation under an external electric field and the orderly arrangement of ferroelectric domains, thereby enhancing the piezoelectric response of ceramics [24]. The stripe domains correspond to the 90° ferroelectric domain wall, and the polarizations in the adjacent domains are arranged at the beginning and end of the domain wall. Both sides of the herringbone pattern are formed by many parallel stripes at an angle of nearly 90° [25]. The stripe and herringbone domains are usually reported to be typical features of the domain configuration for $BaTiO_3$ ceramics with tetragonal symmetry. These materials are highly sensitive to the applied external electric field, which is conducive to polarization switching and can significantly improve the piezoelectric effect [26,27]. Furthermore, the interplanar spacing of 0.28 nm in the HRTEM image corresponds to both the (110) and (101) crystal planes of BCTZ (JCPDs No. 85-0368), as displayed in Fig. 2(c). The corresponding SAED patterns in Fig. 2(d) provided further confirmation of the high crystallinity.

The crystal structures of the BCTZ–*x*SiC ceramics were investigated via XRD patterns, as shown in Fig. 3(a). A pure perovskite structure without any impurities was observed, indicating that the doped elements were completely immersed in the BCTZ–0SiC ceramics. A small diffraction peak near 30° indexed to SiO_2 (PDF#75-1381) was found for the BCTZ–0.2SiC ceramic, as shown in Fig. 3(b), which indicated that SiC transformed into SiO_2 during the high-temperature sintering process because of the instability of SiC in air. The incomplete splitting of the (200) diffraction peaks proved that the BCTZ–*x*SiC ceramic sample was located in the multiphase coexistence region with rhombohedral (R), orthorhombic (O), and tetragonal (T) phases [28,29]. The (002)/(200) XRD peaks at approximately 45°–45.5° are displayed in Fig. 3(c). The peak position shifted to a higher angle with increasing SiC content, indicating that the ABO_3 lattice shrank. Considering the radii of the Si^{4+} (0.42 Å), Zr^{4+} (0.605 Å), and Ti^{4+} (0.72 Å) ions, it was suggested that Si ions tended to enter the B-site in the ABO_3 lattice.

To further explore the influence of SiC on the crystal structure of the BCTZ–*x*SiC ceramic samples, we performed Rietveld refinement on the XRD patterns with the assistance of GSAS software (version 2.0). Figure 3(d) shows the Rietveld refinement XRD patterns of the BCTZ–0.1SiC ceramics with rhombohedral (*R3m*) (PDF#85-0368), orthorhombic (*Amm*2) (PDF#81-2200), and tetragonal (*P4mm*) (PDF#79-2265) crystal structures. The other XRD refinement results are shown in Fig. S3 in the ESM. The refinement parameters and lattice parameters of the BCTZ–*x*SiC ceramics are summarized in Table S1 in the ESM. The calculated lines fit very well with the experimental lines, and all the refined fitting parameters—weighted profile residual (R_{wp}) and diffraction line profile residual (R_p) values were less than 10%, proving that the fitting results were reliable. All the ceramic samples located at MPB were composed of rhombohedral, orthorhombic, and tetragonal phases. In addition, the lattice parameters generally decreased as the SiC content increased, which indicated the incorporation of Si ions into the ABO_3 lattice. The atomic coordinates of the BCTZ–*x*SiC ceramics, as summarized in Table S2 in the ESM, also confirmed the entrance

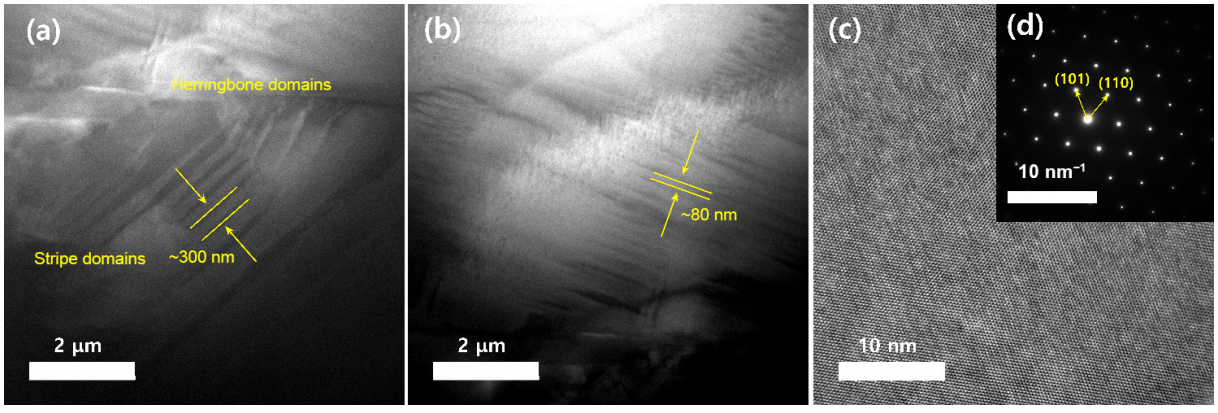

Fig. 2 (a, b) Bright-field TEM images, (c) HRTEM image, and (d) SAED pattern of BCTZ–0.1SiC ceramic samples.

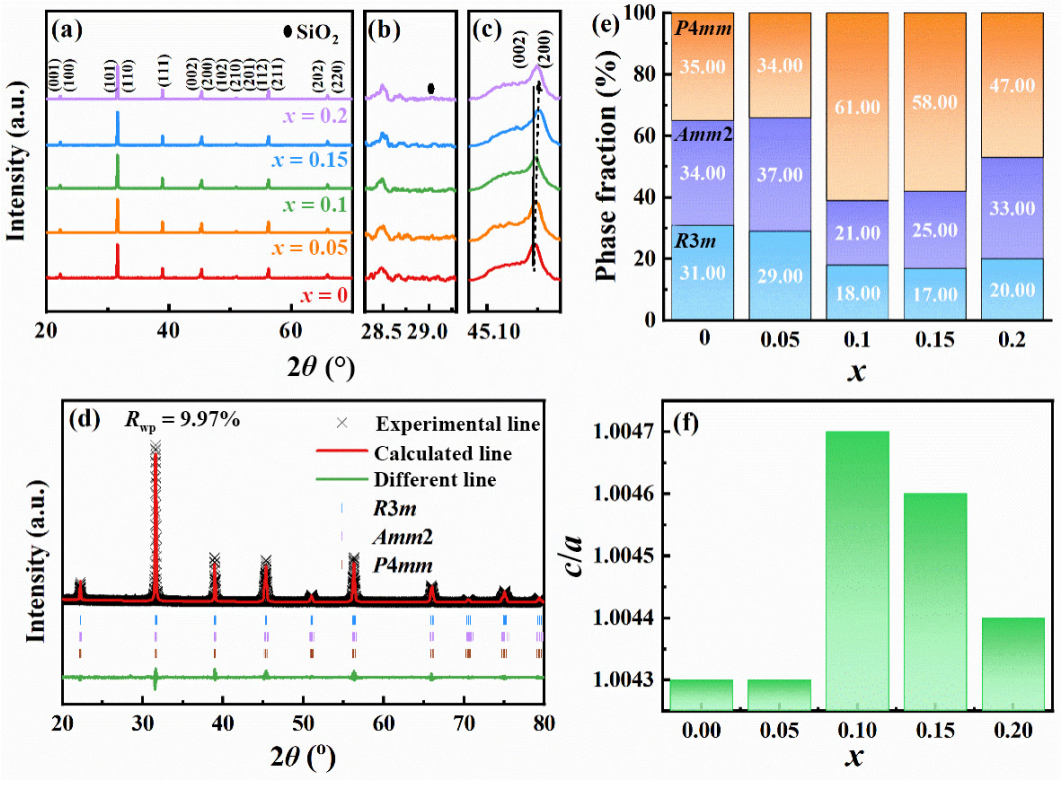

Fig. 3 (a) XRD patterns, (b) magnified diffraction peaks in 2θ range of 28.3°–29.3°, and (c) magnified (002)/(200) diffraction peaks of BCTZ–xSiC samples. (d) XRD Rietveld refinement results for x = 0.1 sample. (e) Phase fractions of BCTZ–xSiC ceramic samples. (f) c/a of BCTZ–xSiC ceramics as a function of x.

of Si into the lattice. According to Fig. 3(e), with increasing SiC doping amount, the proportion of the tetragonal phase first increased but then decreased, and the maximum value was obtained for the BCTZ–0.1SiC ceramics, for which the proportion of the tetragonal phase reached 61%. The tetragonal phase had a large c-axis, where the B-site ions underwent a large relative displacement so that the tetragonal phase exhibited a strong spontaneous polarization ability [8]. XRD analysis revealed that the doping of SiC affected the crystal structure and then changed the proportion of the phase structure due to the occupation of Si ions in the ABO_3 lattice. The ratio of c to the lattice constant (c/a) of the tetragonal phase is summarized in Fig. 3(f) and Table S1 in the ESM. c/a represents the displacement distance of B-site ions in the ABO_3 perovskite lattice, which directly affects the piezoelectric properties. c/a first increased and then decreased, and the maximum value was obtained at x = 0.1, indicating that SiC can not only increase the lattice distortion but also increase the displacement distance of B-site ions when x > 1, which is conducive to achieving an excellent piezoelectric response.

To further elucidate the crystal structure of the BCTZ–xSiC ceramics, six points were randomly selected from the Raman images in Figs. 4(a)–4(d) of the ceramic sample and the Raman spectra in the frequency range of 100–1000 cm^{-1} were plotted, as shown in Fig. 4(e). The seven vibration Raman bands ν_1–ν_7 represented $A(TO_1)$, $A(TO_2)$, B(TO + LO), E(TO + LO), E(TO) + $A(LO_1)$, $A(TO_3)$/E(TO) , and A(LO)/E(LO) [30], respectively. The wave bands at low frequencies are associated mainly with the vibration of the A-site in perovskite ceramics, and those at high frequencies are due to the vibration of the TiO_6 octahedron [31]. The main characteristics of the Raman spectra, such as ν_6 and ν_7, were consistent with the tetragonal phase of $BaTiO_3$ [32]. ν_2 generally exists in rhombohedral and tetragonal phases [33]. ν_3 confirmed the coexistence of rhombohedral and tetragonal phases [34]. The ceramic samples had a multiphase coexistence

structure at room temperature. In addition, the Raman shift at 437 cm^{-1} clearly displaced, indicating that there was stress in the ceramic sample [35]. The main reason was that Si^{4+} ions with smaller ion radii entered the crystal lattice, resulting in lattice shrinkage and, thus stress in the ceramic. When the lattice strain energy reached or exceeded the formation energy of the defect, the pressure was released, accompanied by the generation of defects, which was confirmed by the following impedance spectra.

Figure 5(a) shows the ε_r and tanδ values of the BCTZ–xSiC ceramics as a function of temperature in the range from −50 to 200 °C measured at a fixed frequency of 1 kHz. The dependences of ε_r and tanδ on temperature at different frequencies are shown in Fig. S4 in the ESM. There were three dielectric constant anomalies, which correspond to the rhombohedral–orthorhombic phase transition, orthorhombic–tetragonal phase transition, and Curie temperature over the measured temperature range. With increasing SiC content, the phase transition temperature remained almost unchanged, as shown in Fig. 5(b), indicating that doping SiC had little influence on the crystal structure. All the samples maintain high T_c of ~95 °C. The broadened rhombohedral–orthorhombic and orthorhombic–tetragonal phase transitions near room temperature indicated that the systems located in the rhombohedral–orthorhombic–tetragonal three-phase coexisted with the XRD analysis. The construction of an MPB at room temperature was beneficial for reducing the Landau-free energy and the anisotropy among multiple phases [36], which was conducive to domain switching. The coexistence of multiple phases at room temperature was the fundamental reason for the high piezoelectric properties in this work. In addition, the tanδ values of all the ceramic samples are low. This meant that the defect concentration of the ceramics was low, which improved the piezoelectric properties.

The impedance spectra of all the compositions at 400 °C are presented in Fig. 6(a), with test frequencies ranging from 20 Hz to 1 MHz. Figure S5 in the ESM shows the impedance spectra of the BCTZ–xSiC ceramics measured from 400 to 475 °C. The samples had two different typical semicircles, where the former at high frequency was generated by the grain effect, and the latter at low frequency represented the contributions of the grain boundaries. Compared with the other samples, the BCTZ–0.1SiC sample had a relatively large radius, indicating that it had the highest resistivity. To obtain the detailed grain resistance (R_g), grain boundary resistance (R_{gb}), grain capacitance (CPE_g), and grain boundary capacitance (CPE_{gb}), we used the equivalent fitting circuit shown in the embedded diagram in Fig. 6(a) to accurately distinguish the contributions of the grains and grain boundaries. The fitted grain and grain boundary resistance values at different temperatures are summarized in Table S3 in the ESM. The grain resistance is generally greater than the grain boundary resistance, implying that the migration of defect carriers within grains is more difficult than that within grain boundaries. Both R_g and R_{gb} first increased and then decreased, reaching a maximum in the BCTZ–0.1SiC ceramics, which demonstrated the lowest oxygen vacancy concentration in the BCTZ–0.1SiC ceramics. To further confirm the oxygen vacancy concentration in the BCZT–xSiC ceramics, high-resolution O 1s XPS spectra were collected, as

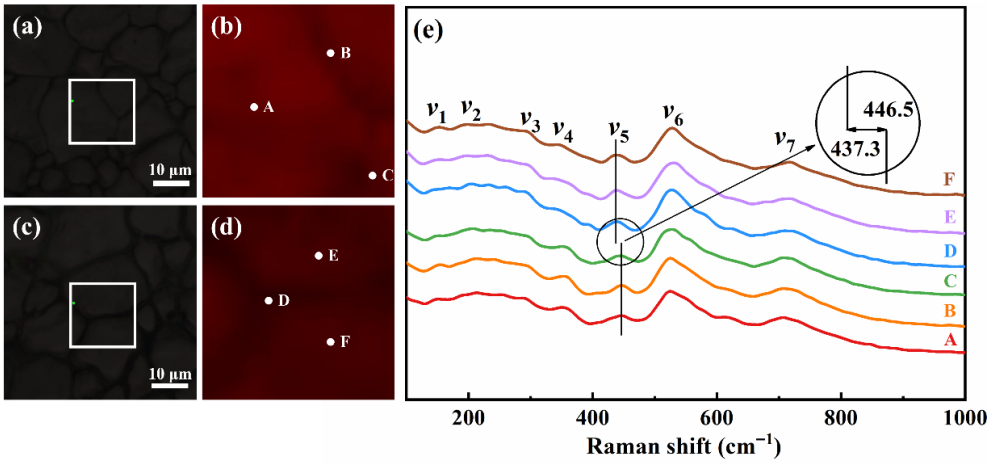

Fig. 4 (a) Raman microscopy surface image and (b) amplified image of BCTZ–0SiC. (c) Raman microscopy surface image and (d) amplified image of BCTZ–0.1SiC. (e) Raman spectra of corresponding points.

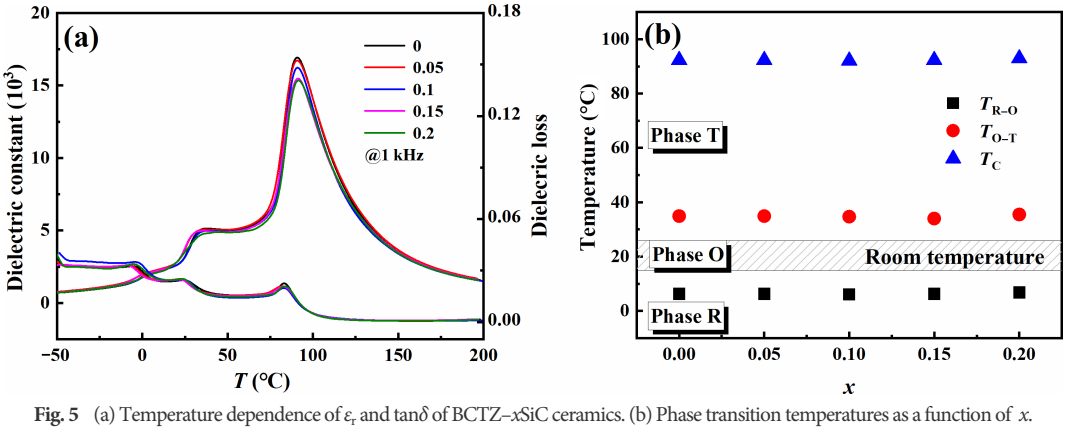

Fig. 5 (a) Temperature dependence of ε_r and tanδ of BCTZ–xSiC ceramics. (b) Phase transition temperatures as a function of x.

shown in Fig. 6(c). Each O 1s spectrum was fitted with three peaks representing lattice oxygen ions (O1), oxygen vacancies (O2), and adsorbed oxygen (O3). The peak area ratios are given in Fig. 6(c). The variation in the oxygen vacancy concentration was consistent with the impedance spectra results, and the lowest defect concentration was obtained when $x = 0.1$ [37,38].

After fitting, the conductivity of the sample conformed to the Arrhenius behavior. The activation energy (E_a) was calculated via the Arrhenius formula (Eq. (1)):

$$\sigma = \sigma_0 \exp\left(\frac{-E_a}{k_B T}\right) \quad (1)$$

where σ_0 is the high-temperature limit of conductivity, σ is the conductivity at the measured temperature, E_a is the activation energy, k_B is the Boltzmann constant, and T is the Kelvin temperature. The E_a values calculated via the formula are summarized in Fig. 6(b), where E_g represents the grain activation energy, and E_{gb} represents the grain boundary activation energy. E_g and E_{gb} first increased and then decreased with increasing x. In the BCTZ–0.1SiC ceramics, the maximum values of the activation energy were obtained, where the E_g and E_{gb} values were 2.18 and 2.54 eV, respectively. The activation energy usually indicates the minimum energy required for the transition of long-range carriers from a metastable state to an excited state [39]. A higher activation energy means more difficult migration for internal electrons and oxygen vacancies in perovskite oxides [40,41], which significantly improves the insulation performance. When $x = 0.1$, the migration ability of the surface carriers was the lowest, and the insulation performance was the highest.

The largest E_a at $x = 0.1$ corresponded to the lowest oxygen vacancy concentration. When the undoped BCTZ ceramics were sintered at high temperature, the lattice oxygen ($O_O^{\times}$) escaped during the sintering process because of the high sintering temperature, accompanied by the generation of oxygen vacancies ($V_O^{\cdot\cdot}$) and free electrons (e'). The equation is expressed as Reaction (2):

$$O_O^{\times} \leftrightarrow \frac{1}{2}O_2 \uparrow + V_O^{\cdot\cdot} + 2e' \quad (2)$$

Therefore, the pure BCTZ ceramics presented a large E_a value and high oxygen vacancy concentration. After SiC was doped into the BCTZ ceramics, some Si^{4+} ions entered the A-site to replace Ba^{2+} and Ca^{2+} ions according to the XRD analysis. It formed an A-site point defect ($Si_A^{\cdot\cdot}$) and stable lattice oxygen, accompanied by CO_2 production. The equation is as Reaction (3):

$$SiC + 2O_2 + 2V_O^{\cdot\cdot} \rightarrow Si_A^{\cdot\cdot} + CO_2 \uparrow + 2O_O^{\times} \quad (3)$$

This process reduces the oxygen vacancy concentration and increases E_a. Nevertheless, the entrance of Si^{4+} ions in the A-site deformed the crystal lattice due to the smaller ion radius compared with those of the other A-site ions, resulting in internal stress in the ceramic, as verified by the Raman spectra. When the lattice strain energy reached or exceeded the formation energy of the defect, the stress was released, accompanied by the generation of defects. Therefore, the defect concentration increased, and E_a decreased when $x > 0.1$.

Figures 7(a)–7(c) present the P–E hysteresis loops and S–E curves under a fixed electric field of 4 kV/mm and a fixed frequency of 1 Hz. All the samples exhibited a saturated hysteresis

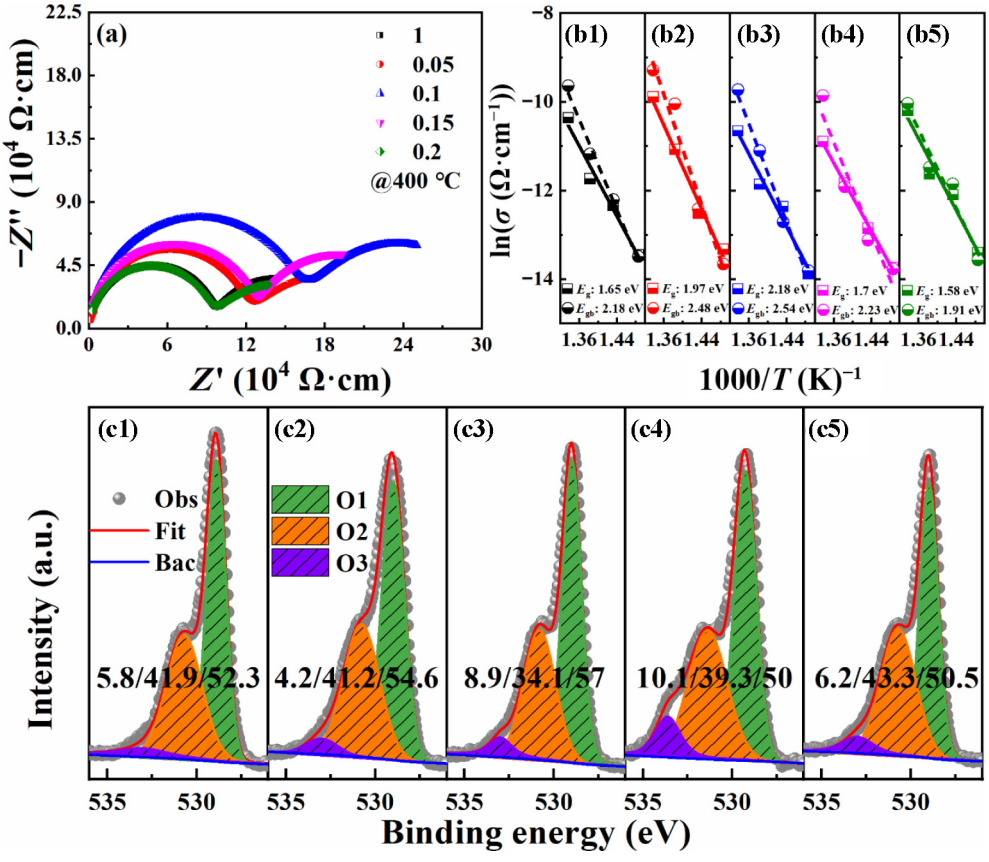

Fig. 6 (a) Impedance spectra of BCTZ–xSiC ceramics at 400 °C and corresponding equivalent circuit. Arrhenius plots and corresponding fitted activation energies of (b1) BCTZ–0SiC, (b2) BCTZ–0.05SiC, (b3) BCTZ–0.1SiC, (b4) BCTZ–0.15SiC, and (b5) BCTZ–0.2SiC. XPS spectra of (c1) BCTZ–0SiC, (c2) BCTZ–0.05SiC, (c3) BCTZ–0.1SiC, (c4) BCTZ–0.15SiC, and (c5) BCTZ–0.2SiC.

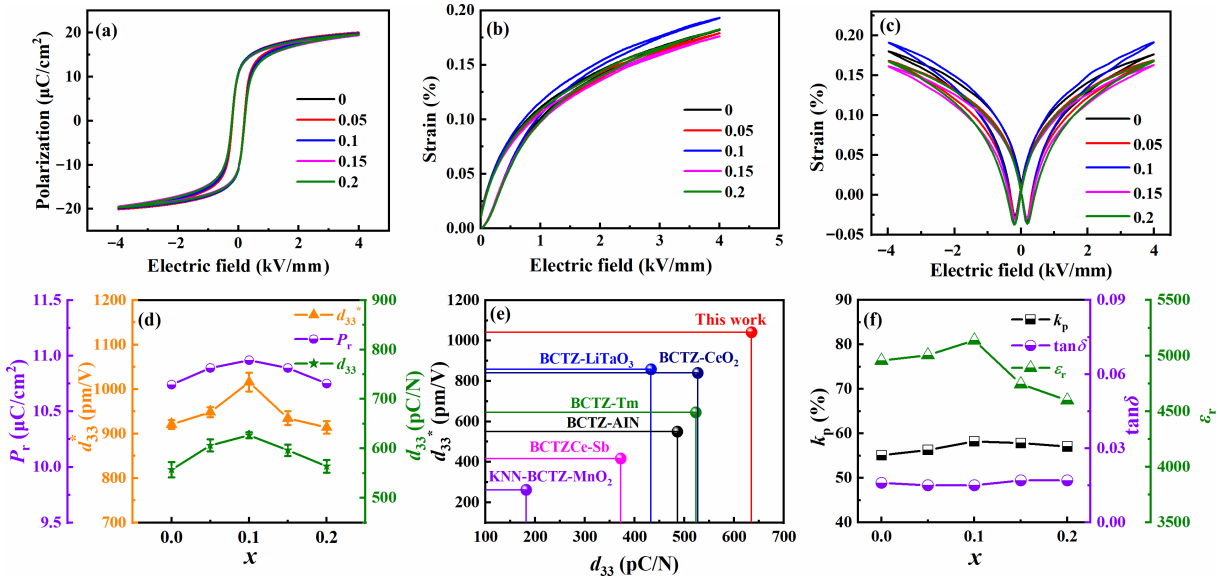

Fig. 7 (a) *P*–*E* loops, (b) unipolar *S*–*E* curves, and (c) bipolar *S*–*E* loops measured at a frequency of 1 Hz and an applied electric field of 40 kV/mm. (d) d_{33}, d_{33}*, and P_r as a function of *x*, where error bars represent standard error of mean. (e) Comparison of d_{33} and d_{33}* in this work with those of other reported BCTZ-based piezoelectric ceramics. (f) k_p, ε_r, and tanδ of BCZT–*x*SiC ceramics as a function of *x*.

loop, indicating their good ferroelectric properties. As shown in Fig. 7(d), the remnant polarization (P_r) of the ceramic samples first increased but then decreased, reaching a maximum of 10.96 μC/cm² when $x = 0.1$. The increase in P_r was due mainly to the large grain size and improved compactness of the ceramics. However, when SiC doping was excessive, the ferroelectric properties deteriorated because the generated secondary phase SiO_2 was non ferroelectric.

The converse piezoelectric coefficient (d_{33}*), an important parameter for evaluating piezoelectric properties, is the deformation of piezoelectric ceramics under the action of an external electric field and can be calculated via the formula $d_{33}^* = S_{max}/E_{max}$, where S_{max} represents the maximum strain, and E_{max} represents the maximum measured electric field. As shown in Fig. 7(d), d_{33}* of the ceramic sample first increased but then decreased, reaching a maximum of 1048 pm/V in the BCTZ–0.1SiC ceramics. d_{33}* is generally derived from intrinsic contributions and extrinsic contributions [24]. The intrinsic contribution was related mainly to lattice distortion. The constructed MPB in the BCTZ–0.1SiC sample at room temperature was beneficial for reducing the Landau-free energy and the anisotropy among multiple phases, which was conducive to domain switching. In addition, the incorporation of Si^{4+} in the B-site of the ABO_3 lattice deformed the crystal structure and enhanced the lattice distortion, which improved the piezoelectric response. The extrinsic contribution is related to domain switching and domain wall motion under large external electric fields. The refined domain configurations with an average size of approximately 80 nm in Fig. 2(b) could facilitate the polarization orientation under an external electric field and the orderly arrangement of ferroelectric domains, thereby enhancing the piezoelectric response of ceramics. The piezoelectric characteristics of the BCTZ–*x*SiC ceramics measured at room temperature are summarized in Figs. 7(e) and 7(f). With increasing SiC content, d_{33} reached a maximum of 638 pC/N for $x = 0.1$, accompanied by the highest k_p of 58.21%. Compared with the other reported BT-based ceramics, as summarized in Fig. 7(e) [8,17,42–50], the piezoelectric performance in this work was significantly improved. However, when $x > 0.1$, the piezoelectric properties tended to degrade. The ε_r tended to increase to the maximum value when $x < 0.1$ and then decreased consistently. The tanδ for all the composites was relatively low, at < 0.02, demonstrating that the ceramic samples had compact microstructures and excellent insulation resistivity.

The enhancement in the piezoelectric and ferroelectric properties of the $x = 0.1$ ceramics is multifaceted, as depicted in Fig. 8. First, compared with $BaTiO_3$ (215 W/(m·K)), doped SiC has an excellent thermal conductivity of 300–500 W/(m·K) [18,19]. The heat was rapidly transferred to the BCTZ grains through the SiC particles, which promoted mass transport and grain growth and improved the compactness of the ceramic samples. Large grains can significantly reduce the activation energy of domain wall motion due to the external effects of grain boundaries, contributing to a high piezoelectric response [51]. In addition, according to the grain size effect model, a decrease in the grain size led to an increase in the grain boundary ratio and a corresponding strong pinning effect [52,53]. Second, the BCZT–*x*SiC ceramics are located in the MPB region and possess abundant polarization directions since the R phase has eight polarization directions, the O phase has six polarization directions, and the T phase has six polarization directions, which is conducive to domain switching and thus enhances the piezoelectric response [54,55]. Compared with those of the other counterparts, the *c*/*a* ratio and lattice distortion for the $x = 0.1$ ceramics were greater, which promoted the displacement of B-site ions (*c*/*a* of the tetragonal phase) in response to the external field, thus enhancing the piezoelectric and ferroelectric responses [54]. Third, the incorporation of Si^{4+} could reduce the oxygen vacancy

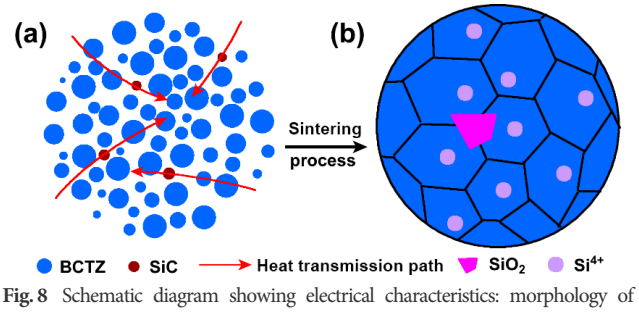

Fig. 8 Schematic diagram showing electrical characteristics: morphology of sample (a) before and (b) after sintering process.

concentration and charge carrier activation energy, which softened the piezoelectric properties and increased the ferroelectric activity [56]. The significant decline in both the piezoelectric and dielectric properties when x surpassed 0.1 was associated with intense internal stresses from small grains and a pronounced pinning effect due to defect dipoles. The deterioration of piezoelectric properties when $x > 0.1$ was also related to the reduced grain size because of the increased proportion of nonferroelectric grain boundaries and clamping effects of the domain walls.

The temperature stability is a key parameter for evaluating the application of piezoelectric ceramics. The temperature-dependent P–E loops and unipolar S–E curves of the $x = 0$ and 0.1 samples are depicted in Figs. 9(a) and 9(b) and Figs. 9(c) and 9(d), respectively. The normalized P_r and the normalized unipolar strain (S_{uni}) are represented as $P_{r(T)}/P_{r(RT)}$ and $S_{uni(T)}/S_{uni(RT)}$ (T is the measurement temperature, and RT is the room temperature), respectively, as summarized in Figs. 9(e) and 9(f). On the one hand, the hysteresis loops tended to shrink with increasing temperature; that is, P_r and S_{uni} decreased, which was because the thermal fluctuations at high temperatures destroyed the long-range order. On the other hand, P_r and strain of the BCTZ–0.1SiC ceramics were greater than those of the BCTZ–0SiC ceramics. For the BCTZ–0.1SiC ceramic samples, when the temperature increased from 30 to 80 °C, P_r decreased from 10.96 to 5.34 μC/cm^2, with a retention rate of 48.7%. The strain decreased from 0.193% to 0.135%, with a retention rate of 70%. When the test temperature reached 85 °C, the electrical performance decreased significantly. Compared with that of the BCTZ–0SiC ceramic samples, the performance of the BCTZ–0.1SiC ceramics was greater at the same temperature. Obviously, BCTZ–0.1SiC showed a small variation in S_{uni} over a wide temperature range from room temperature to 80 °C, providing a guarantee for the application of ceramics at high temperatures.

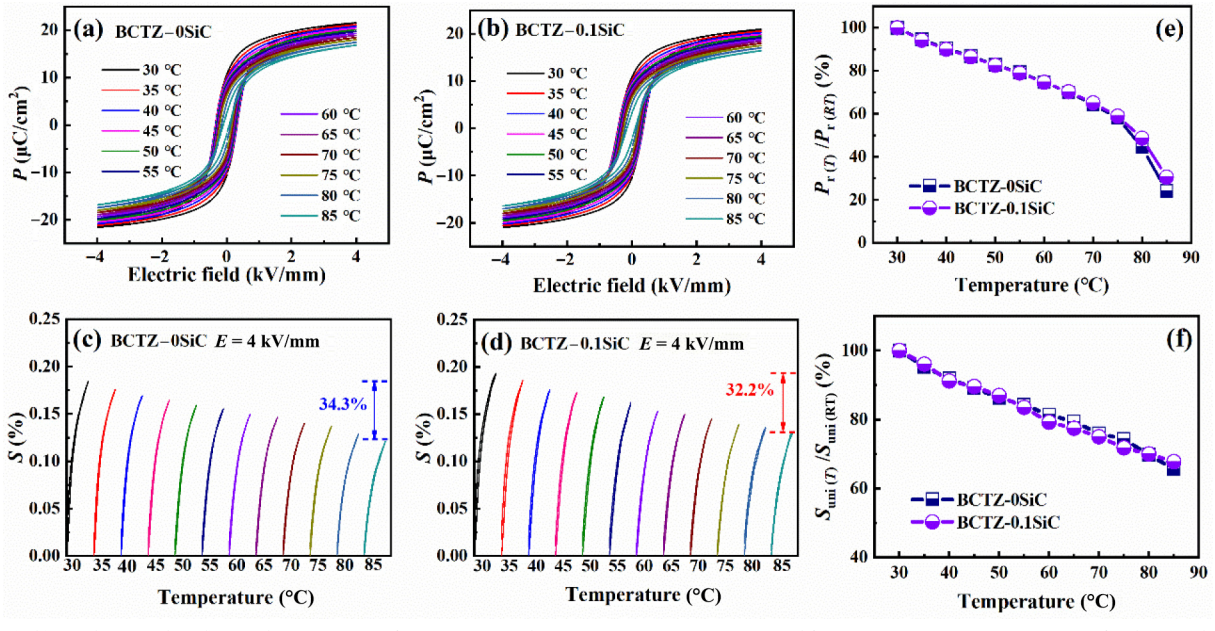

Fig. 9 (a, b) P–E loops and (c, d) unipolar S–E curves of BCTZ–0SiC and BCTZ–0.1SiC ceramics measured from room temperature to 85 °C at a fixed external electric field of 4 kV/mm. Comparison between (e) normalized P_r and (f) normalized unipolar strain (S_{uni})of BCTZ–0SiC and BCTZ–0.1SiC ceramics.

4 Conclusions

In this work, SiC was selected to optimize the phase structure, defect configuration, morphology, and sintering process of BCZT lead-free piezoelectric ceramics. On the one hand, SiC can promote the sintering process and grain growth due to its excellent thermal conductivity, resulting in the compactness of ceramics. On the other hand, the incorporation of Si^{4+} in the B-site of the ABO_3 lattice not only deforms the crystal structure and enhances the lattice distortion but also reduces the oxygen vacancy concentration and increases the charge carrier activation energy. As a result, excellent piezoelectric responses of d_{33} = 638 pC/N, d_{33}* = 1048 pm/V, k_p = 58.21%, and T_c of ~95 °C were achieved at the optimized composition. These experimental results demonstrate that the SiC dopant can effectively adjust the sintering process and optimize the comprehensive electrical performance of BCTZ-based ceramics.

Acknowledgements

The work was supported by the Taishan Scholars Program (No. tsqn202312214), the Natural Science Foundation of Shandong Province (No. ZR2024QE104), the Shandong Province Key Fundamental Research Program (No. ZR2022ZD39), and the Open Foundation of Guangdong Provincial Key Laboratory of Electronic Functional Materials and Devices (No. EFMD2024005Z).

Author contributions

AiHui Yang: Writing-original draft, data curation, validation, methodology; Yu Huan: Writing—review & editing, funding acquisition, supervision, validation; Qingying Wang: Data curation, validation; Ting Wang: Formal analysis, methodology, funding acquisition; Yuanhui Su: Formal analysis, methodology, writing—review & editing; Tao Wei: Supervision, funding acquisition.

Availability of data and materials

The data that support the findings of this study are available from the corresponding author upon reasonable request.

Competing interests

The authors have no competing interests to declare that are relevant to the content of this article. The author Yu Huan is the Editorial Committee member of this journal.

Electronic Supplementary Material

Supplementary material is available in the online version of this article at https://doi.org/10.26599/JAC.2025.9221054.

References

[1] Lv X, Zhu JG, Xiao DQ, *et al.* Emerging new phase boundary in potassium sodium-niobate based ceramics. *Chem Soc Rev* 2020, **49**: 671–707.

[2] Huan Y, Hou LM, Wei T, *et al.* High-performance (K,Na)NbO_3-based multilayer piezoelectric ceramic actuators with nickel inner electrodes. *J Adv Ceram* 2023, **12**: 1228–1237.

[3] Hou LM, Huan Y, Zheng MP, *et al.* 3D vertically aligned microchannel structure to enhance piezoelectric energy harvesting performance of PZT/PVDF&CNTs piezoelectric composites. *J Materiomics* 2024, **10**: 1063–1070.

[4] Huan Y, Wu LZ, Xu LY, *et al.* Superior energy-storage density and ultrahigh efficiency in KNN-based ferroelectric ceramics via high-entropy design. *J Materiomics* 2025, **11**: 100862.

[5] Huan Y, Wang XH, Fang J, *et al.* Grain size effect on piezoelectric and ferroelectric properties of $BaTiO_3$ ceramics. *J Eur Ceram Soc* 2014, **34**: 1445–1448.

[6] Qin HL, Zhao JW, Chen XX, *et al.* Investigation of $BiFeO_3$–$BaTiO_3$ lead-free piezoelectric ceramics with nonstoichiometric bismuth. *Microstructures* 2023, **3**: 2023035.

[7] Hong CH, Kim HP, Choi BY, *et al.* Lead-free piezoceramics–Where to move on. *J Materiomics* 2016, **2**: 1–24.

[8] Wang XJ, Huan Y, Ji SJ, *et al.* Ultra-high piezoelectric performance by rational tuning of heterovalent-ion doping in lead-free piezoelectric ceramics. *Nano Energy* 2022, **101**: 107580.

[9] Liu WF, Ren XB. Large piezoelectric effect in Pb-free ceramics. *Phys Rev Lett* 2009, **103**: 257602.

[10] Chen XM, Li YS, Zeng JT, *et al.* Phase transition and large electro strain in lead-free Li-doped (Ba,Ca)(Ti,Zr)O_3 ceramics. *J Am Ceram Soc* 2016, **99**: 2170–2174.

[11] Xue A, Liu QB, Yang HP, *et al.* Rhombohedral-orthorhombic-tetragonal multiphases coexist in $(Ba_{0.85}Ca_{0.15})(Ti_{0.9}Zr_{0.08}Sn_{0.02})O_3$–$SrTiO_3$ piezoelectric ceramics prepared by microwave sintering techniques. *J Mater Sci: Mater El* 2020, **31**: 19388–19395.

[12] Wu B, Zheng HJ, Wu YQ, *et al.* Origin of ultrahigh-performance barium titanate-based piezoelectrics: Stannum-induced intrinsic and extrinsic contributions. *Nat Commun* 2024, **15**: 7700.

[13] Benabdallah F, Elissalde C, Seu UCC, *et al.* Structure–microstructure–property relationships in lead-free BCTZ piezoceramics processed by conventional sintering and spark plasma sintering. *J Eur Ceram Soc* 2015, **35**: 4153–4161.

[14] Orlik K, Lorgouilloux Y, Marchet P, *et al.* Influence of microwave sintering on electrical properties of BCTZ lead free piezoelectric ceramics. *J Eur Ceram Soc* 2020, **40**: 1212–1216.

[15] Nahas Y, Akbarzadeh A, Prokhorenko S, *et al.* Microscopic origins of the large piezoelectricity of lead free (Ba,Ca)(Zr,Ti)O_3. *Nat Commun* 2017, **8**: 15944.

[16] Wang L, Zhang FQ, Chen C, *et al.* Bandgap engineering of BZT–BCT by Mn doping and the emerging strong photo-pyroelectric effect. *Nano Energy* 2024, **119**: 109081.

[17] Chen T, Zhang T, Wang GC, *et al.* Effect of CuO on the microstructure and electrical properties of $Ba_{0.85}Ca_{0.15}Ti_{0.90}Zr_{0.10}O_3$ piezoceramics. *J Mater Sci* 2012, **47**: 4612–4619.

[18] Chelnokov VE, Syrkin AL. High temperature electronics using SiC: Actual situation and unsolved problems. *Mater Sci Eng B* 1997, **46**: 248–253.

[19] He Y. Heat capacity, thermal conductivity, and thermal expansion of barium titanate-based ceramics. *Thermochim Acta* 2004, **419**: 135–141.

[20] Zhang Z, Cao LH, Zhi SH, *et al.* Influences of sintering temperature on structures of lead magnesium niobate-lead zirconate titanate piezoelectric ceramics. *China Powder Sci Technol* 2010, **16**: 65–68. (in Chinese)

[21] Chen H, Yang H, Dong XL, *et al.* Properties of PZT/SiC composites processed by solid state diffusion. *Phys Status Solidi A* 2006, **203**: R61–R63.

[22] Sun XX, Zhang JW, Lv X, *et al.* Understanding the piezoelectricity of high-performance potassium sodium niobate ceramics from diffused multi-phase coexistence and domain feature. *J Mater Chem A* 2019, **7**: 16803–16811.

[23] Huan Y, Wang XH, Fang J, *et al.* Grain size effects on piezoelectric properties and domain structure of $BaTiO_3$ ceramics prepared by two-step sintering. *J Am Ceram Soc* 2013, **96**: 3369–3371.

[24] Huan Y, Wang XH, Li LT, *et al.* Strong domain configuration dependence of the nonlinear dielectric response in (K,Na)NbO_3-based ceramics. *Appl Phys Lett* 2015, **107**: 202903.

[25] Luan SW, Guo R, Zhang L, *et al.* Study on the synergistic effect of Dy and Ho rare earths on the dielectric properties of X9R $BaTiO_3$-based ceramic. *Adv Ceram* 2024, **45**: 530–540. (in Chinese)

[26] Le DT, Kwon SJ, Yeom NR, *et al.* Effects of the domain size on local d_{33} in tetragonal $(Na_{0.53}K_{0.45}Li_{0.02})(Nb_{0.8}Ta_{0.2})O_3$ ceramics. *J Am Ceram Soc* 2013, **96**: 174–178.

[27] Huan Y, Wei T, Wang ZX, *et al.* Polarization switching and rotation in KNN-based lead-free piezoelectric ceramics near the polymorphic phase boundary. *J Eur Ceram Soc* 2019, **39**: 1002–1010.

[28] Mittal S, Laishram R, Singh KC. Multi-phase coexistence in yttrium-substituted $Ba_{0.9}Ca_{0.1}Zr_{0.07}Ti_{0.93}O_3$ lead-free piezoceramics. *Ceram Int* 2019, **45**: 1237–1245.

[29] Wang XJ, Huan Y, Zhu YX, *et al.* Defect engineering of BCZT-based piezoelectric ceramics with high piezoelectric properties. *J Adv Ceram* 2022, **11**: 184–195.

[30] Guo HZ, Chen ZH, Cheng BL, *et al.* Structure dynamics of strongly reduced epitaxial $BaTiO_{3-x}$ studied by Raman scattering. *J Eur Ceram Soc* 2005, **25**: 2347–2352.

[31] Li Y, Cheng HB, Xu HW, *et al.* Electromechanical properties of (Ba, Sr)(Zr,Ti)O_3 ceramics. *Ceram Int* 2016, **42**: 10191–10196.

[32] Wang H, Yuan H, Hu Q, *et al.* Exploring the high-performance (1–x) $BaTiO_{3-x}$–$CaZrO_3$ piezoceramics with multiphase coexistence (R–O–T) from internal lattice distortion and domain features. *J Alloys Compd* 2021, **853**: 157167.

[33] Janbua W, Bongkarn T, Kolodiazhnyi T, *et al.* High piezoelectric response and polymorphic phase region in the lead-free piezoelectric $BaTiO_3$–$CaTiO_3$–$BaSnO_3$ ternary system. *RSC Adv* 2017, **7**: 30166–30176.

[34] Zhang YM, Deng HM, Si SF, *et al.* Band gap narrowing and magnetic properties of transition-metal-doped $Ba_{0.85}Ca_{0.15}Ti_{0.9}Zr_{0.1}O_3$ lead-free ceramics. *J Am Ceram Soc* 2020, **103**: 2491–2498.

[35] Anastassakis E, Cantarero A, Cardona M. Piezo-Raman measurements and anharmonic parameters in silicon and diamond. *Phys Rev B* 1990, **41**: 7529–7535.

[36] Yan XD, Zheng MP, Gao X, *et al.* High-performance lead-free ferroelectric BZT–BCT and its application in energy fields. *J Mater Chem C* 2020, **8**: 13530–13556.

[37] Li ZH, Roscow J, Khanbareh H, *et al.* Porous structure enhances the longitudinal piezoelectric coefficient and electromechanical coupling coefficient of lead-free $(Ba_{0.85}Ca_{0.15})(Zr_{0.1}Ti_{0.9})O_3$. *Adv Sci* 2024, **11**: 2406255.

[38] Huan Y, Gui DY, Li CX, *et al.* Simultaneously enhanced energy storage performance and luminance resistance in $(K_{0.5}Na_{0.5})NbO_3$-based ceramics via synergistic optimization strategy. *J Adv Ceram* 2024, **13**: 34–43.

[39] Wang XZ, Huan Y, Wang ZX, *et al.* Electrical conduction and

dielectric relaxation mechanisms in the KNN-based ceramics. *J Appl Phys* 2019, **126**: 104101.

[40] Guo X. Peculiar size effect in nanocrystalline $BaTiO_3$. *Acta Mater* 2013, **61**: 1748–1756.

[41] Huan Y, Ma MY, Su YH, *et al.* Environmentally regulated intrinsic oxygen-ion transport for oxide-ion conductors. *J Materiomics* 2023, **9**: 867–873.

[42] Bai WF, Wang LJ, Zheng P, *et al.* Electromechanical response and piezoelectric properties in $(Ba_{0.85}Ca_{0.15})(Zr_{0.1}Ti_{0.9})O_3$ piezoceramics using nano-sized AlN modification. *Ceram Int* 2018, **44**: 16040–16050.

[43] Hao JG, Li W, Bai WF, *et al.* Phase structures and electrical properties of $(1-x)(K_{0.48}Na_{0.52})NbO_3$–$x(Ba_{0.85}Ca_{0.15})(Zr_{0.1}Ti_{0.9})O_3$ lead-free ceramics. *Ceram Int* 2013, **39**: S685–S689.

[44] Li QT, Zhang QW, Cai W, *et al.* Enhanced ferroelectric and piezoelectric responses of $(Ba_{0.85}Ca_{0.15})(Zr_{0.1}Ti_{0.9})O_3$ ceramics by Tm^{3+} amphoteric substitution. *Mater Chem Phys* 2020, **252**: 123242.

[45] Bijalwan V, Hughes H, Pooladvand H, *et al.* The effect of sintering temperature on the microstructure and functional properties of BCZT-$x$$CeO_2$ lead free ceramics. *Mater Res Bull* 2019, **114**: 121–129.

[46] Zhou MX, Liang RH, Zhou ZY, *et al.* Enhanced Curie temperature and piezoelectric properties of $(Ba_{0.85}Ca_{0.15})(Zr_{0.10}Ti_{0.90})O_3$ lead-free ceramics after the addition of $LiTaO_3$. *Mater Res Bull* 2018, **106**: 213–219.

[47] Zheng WJ, Lin JQ, Liu XM, *et al.* Enhanced ferroelectric and piezoelectric performance of $(Ba_{0.85}Ca_{0.15})(Zr_{0.1}Ti_{0.9})O_3$ lead-free ceramics upon Ce and Sb co-doping. *RSC Adv* 2021, **11**: 2616–2623.

[48] Chen XM, Ruan XZ, Zhao KY, *et al.* Low sintering temperature and high piezoelectric properties of Li-doped (Ba,Ca)(Ti,Zr)O_3 lead-free ceramics. *J Alloys Compd* 2015, **632**: 103–109.

[49] Huang XY, Gao CH, Huang MS, *et al.* Influence of co ion doped amount on property of BCTZ piezoelectric ceramics sintered at low temperature. *Ferroelectrics* 2015, **481**: 146–154.

[50] Ma JF, Liu XY, Li WH. High piezoelectric coefficient and temperature stability of Ga_2O_3-doped $(Ba_{0.99}Ca_{0.01})(Zr_{0.02}Ti_{0.98})O_3$ lead-free ceramics by low-temperature sintering. *J Alloys Compd* 2013, **581**: 642–645.

[51] Qi XD, Sun EW, Wang JJ, *et al.* Electromechanical properties of Mn-doped $Pb(In_{1/2}Nb_{1/2})O_3$–$Pb(Mg_{1/3}Nb_{2/3})O_3$–$PbTiO_3$ piezoelectric ceramics. *Ceram Int* 2016, **42**: 15332–15337.

[52] Fei X, Lin XJ, Wang C, *et al.* Sb_2O_3-modified lead zirconate titanate piezoelectric ceramics with enhancing piezoelectricity and low loss. *J Am Ceram Soc* 2023, **106**: 501–512.

[53] Wang CL, Hou LM, Huan Y Study on the structure and properties of $(1-x)$KNNS–xBFANZ lead-free piezoelectric ceramics. *Adv Ceram* 2023, **44**: 490–496. (in Chinese)

[54] Huan Y, Wang XH, Li LT. Displacement of Ta–O bonds near polymorphic phase transition in Li-, Ta-, and Sb-modified (K,Na)NbO_3 ceramics. *Appl Phys Lett* 2014, **104**: 242905.

[55] Akdoğan EK, Kerman K, Abazari M, *et al.* Origin of high piezoelectric activity in ferroelectric $(K_{0.44}Na_{0.52}Li_{0.04})$–$(Nb_{0.84}Ta_{0.1}Sb_{0.06})O_3$ ceramics. *Appl Phys Lett* 2008, **92**: 112908.

[56] Wang ZX, Huan Y, Wang HZ, *et al.* The optimal sintering atmosphere and defect structure of CuO-doped NKN-based ceramic with p/n-type conduction mechanism. *J Mater Sci Mater El* 2021, **32**: 1928–1940.